BNL-226350-2024-JAAM

Template-Assisted Growth of High-Quality α-Phase FAPbI3 Crystals in Perovskite Solar Cells Using Thiol-Functionalized MoS2 Nanosheets

Y. Yin, Y. Zhang

To be published in "ACS Nano"

October 2024

Center for Functional Nanomaterials

Brookhaven National Laboratory

U.S. Department of Energy

USDOE Office of Science (SC), Basic Energy Sciences (BES). Scientific User Facilities (SUF)

DISCLAIMER

Template-Assisted Growth of High-Quality α-phase $FAPbI_3$ Crystals in Perovskite Solar Cells Using Thiol-Functionalized MoS_2 Nanosheets

Yifan Yin[1], Yuchen Zhou[1], Shi Fu[1], Yu-Chung Lin[1], Xianghao Zuo[1], Aniket Raut[1], Yugang Zhang[2], Esther H. R. Tsai[2], Mingxing Li[2], Fang Lu[2], Chenyu Zhou[2], Tai-De Li[3], Kim Kisslinger[2], Mircea Cotlet[2], Chang-Yong Nam[1,2,], Miriam H. Rafailovich[1,*]*

[1]Department of Material Science and Chemical Engineering, Stony Brook University, Stony Brook, NY 11794, United States

[2]Center for Functional Nanomaterials, Brookhaven National Laboratory, Upton, New York, 11973, United States

[3]Advanced Science Research Center at the Graduate Center of City University of New York, New York 10031, United States

*Corresponding Authors: cynam@bnl.gov (C.-Y.N.), miriam.rafailovich@stonybrook.edu (M.H.R.)

Abstract

Formamidiunm lead iodide (FAPI) has gained attention for hybrid perovskite solar cell (PSC) applications due to its enhanced stability and narrow bandgap. However, a significant challenge remains in inducing and stabilizing the elusive perovskite "black phase"—photoactive cubic α-FAPI—as the relatively bulky FA^+ cations tend to favor the thermodynamically stable non-photoactive "yellow phase". In this study, we present a templated growth strategy employing thiol-functionalized MoS_2 nanosheets as templates. By introducing 3-mercaptopropionic acid (MPA)-functionalized MoS_2 as a growth template, precise control over crystal formation was achieved, favoring the growth of high-quality α-FAPI films. These advanced templated films exhibited substantial improvements in charge transport properties, efficient light absorption, and enhanced charge extraction. As a result, the PSCs achieved a significantly enhanced power conversion efficiency (PCE) compared to the non-templated control device, increasing from 20.6% to 22.5%. The MoS_2-incorporated device also demonstrated excellent shelf stability, maintaining 91% of the initial PCE even after 1600 hours of storage without device encapsulation.

Keywords

Hybrid perovskite, solar cell, additive, nanosheet, ligand, crystallization, templated growth

Introduction

Perovskite materials have become increasingly popular worldwide due to their exceptional optoelectronic properties, which include high light-absorption coefficient, adjustable bandgap, high carrier mobility, bipolar carrier transport, low exciton binding energy, as well as solution processibility and low cost.[1-4] The hybrid halide perovskite with a general structural formula ABX_3 where $MAPbI_3$ ($CH_3NH_3PbI_3$, MAPI) and $FAPbI_3$ ($HC(NH_2)_2PbI_3$, FAPI) are the typically reported two organic-inorganic hybrid perovskite materials used as light absorbers in PSCs. MAPI has been widely used in PSCs since its initial synthesis in 2009.[5] However, the wide bandgap of MAPI (1.55 eV) limits its light absorption, which can hinder its performance in achieving high photocurrent density for solar cells.[6] Compared with MAPI, cubic α-FAPI (photoactive "black" phase) has a narrower bandgap around 1.48 eV,[7] which fits better with the optimum bandgap value of ~1.4 eV for the maximum PCE of a single-junction solar cell and displays extended light absorption toward the near-infrared (IR). Besides, the high volatility of MA anions leads to an easy degradation of MAPI under thermal stress, while FAPI with higher activation energy for dissociation exhibits better long-term thermal durability.[8]

However, α-FAPI undergoes phase conversion into a non-photoactive, hexagonal δ-FAPI ("yellow" phase) easily under ambient conditions because of the lattice distortions caused by the large radius of FA cation.[9, 10] Meanwhile, α-FAPI and δ-FAPI will grow competitively during the crystallization process, and δ-FAPI is more readily formed than α-FAPI due to its smaller formation energy.[11] Furthermore, the active trap centers within the FAPI film is also known to further reduce the activation energy of the α- to δ-phase transition, hence transitions initiated at the traps gradually spreading throughout the entire film.[12] Therefore, it is crucial to control and minimize the presence of traps during the fabrication of perovskite films to achieve high-performance and stable PSCs based on FAPI.

Additive engineering is one of the most common strategies used for mediating perovskite crystal growth and passivating defect states.[13, 14] Functional additives that can either interact with

the FAPI precursor to form an intermediate phase or passivate the perovskite grain boundary[15, 16] and surface[17] were found useful for obtaining uniform and stable α-FAPI films via tailored interfacial interactions between the additive and FAPI. For example, Masi et al. demonstrated that adding a small quantity of lead sulfide (PbS) quantum dots to the perovskite matrix can produce stable black FAPI films.[18] There, the chemical bonding at the PbS-FAPI interface favored the formation of the α-phase, which was crucial for stability, while the introduction of NMP (N-methyl-2-pyrrolidone) as co-additive increased the number of Pb-O bonds that impede the transformation of α-FAPI to δ-FAPI, thereby enhancing the long-term stability of PSCs under ambient air conditions. Additives with unsaturated groups like S=O and C=O are promising for lowering the free energy of FAPI perovskite nuclei because they anchor onto the nuclei surface to reduce the surface energy of specific facet to achieve oriented growth. Wang et al. prepared a highly oriented FA-MA-mixed perovskite film with enhanced charge transport using amino-functionalized carbon nanotubes (CNT-NH_2) and MACl additives.[19] They proposed that the MACl additive facilitated crystal growth by forming an intermediate phase, while the NH_2 groups of the functionalized CNTs provided additional nucleation sites for crystal growth due to their strong affinity toward Pb^{2+} ions. Because of the reduced surface energy of (110) facets, the as-prepared perovskite films showed a strong (110) orientation. Additionally, the CNT-NH_2 remained in the perovskite layer formed charge carrier transfer networks, promoting the charge transport within devices. These prior studies exemplify that using certain nanomaterials with specific orientations, it is possible to induce the templated crystal growth in perovskite films.

In our study, we developed a template-assisted strategy based on a two-dimensional (2D) material additive to prepare α-FAPI with high crystal quality and preferred orientation. To achieve this, we incorporated exfoliated monolayer MoS_2 nanosheets functionalized with thiol-surfactant into the FAPI perovskite bulk. MoS_2 nanosheets possess unique optical and electrical properties due to their 2D structure, which can lead to enhanced electronic transitions and absorption spectra.[20-22] Thiolated surfactants have been used to modify the properties of MoS_2 nanosheets: The thiol group at one end of the surfactant molecule is expected to anchor to the surface of the nanosheet, while the hydrophilic headgroup at the other end can introduce desired functionality to the material.[23, 24] In this study, 3-mercaptopropionic acid (MPA), a commercially available thiol reagent commonly used as a stabilizer for quantum dots and gold nanoparticles [25, 26], was used to modify the MoS_2 nanosheets in a simple and fast manner. The resulting MPA-

MoS_2 nanosheet dispersion exhibited remarkable stability over an extended period more than several months without agglomeration or precipitation. To gain insights into the crystallization dynamics of α-FAPI with MPA-MoS_2, we performed in-situ and ex-situ grazing-incidence wide-angle X-ray scattering (GIWAXS) measurements during thermal annealing step. Our findings revealed that the inclusion of MPA-MoS_2 promotes the formation of the α-FAPI phase during the annealing process. MPA-MoS_2 acts as a template surface for the adsorption of precursors, serving as a growth template that facilitates an orientated nucleation and growth of α-FAPI. This is consistent with previous studies demonstrating the role of MoS_2 in promoting perovskite crystallization by providing preferential nucleation sites and aiding ion diffusion.[27] The time-of-flight secondary ion mass spectrometry (ToF-SIMS) analysis of the FAPI/MPA-MoS_2 system provided valuable insights into the distribution and predominant accumulation of MPA-MoS_2 at the perovskite/bottom bilayer (bl)-TiO_2 interface. The PSCs with MPA-MoS_2 show a significant increase in PCE, from 20.6% to 22.5%. Furthermore, the non-encapsulated devices exhibited excellent shelf stability, maintaining 91% of the initial PCE after 1600 hours.

Results and Discussion

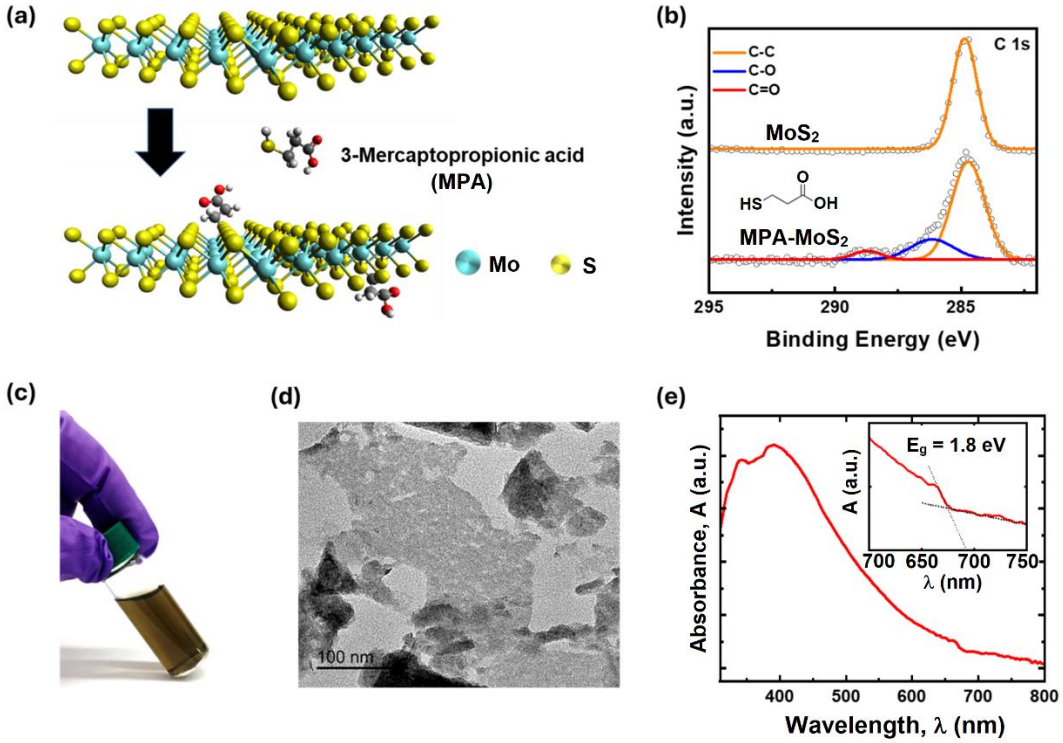

Figure 1. a) Schematic illustration of the synthesis of MPA-MoS_2. b) XPS spectra of pristine MoS_2 and MPA-MoS_2. c) Photograph of MPA-MoS_2 dispersed in DMF. d) TEM image of MPA-MoS_2 nanoflakes. e) Optical absorption spectrum. Inset: calculated optical band gap of the MPA-MoS_2 flakes.

Thiol-functionalized MoS_2 nanosheets (Figure 1a) are synthesized as illustrated in Methods and the Supporting Information. The exfoliation process leads to numerous sulfur deficiencies, which has been reported to possess a high molecular affinity.[28] As previously reported, the HS group at one end acts as an anchor to the nanosheet's surface, while the carboxylic acid (-COOH) group at the opposite end imparts the desired functionality to the material[23, 29]. To provide further insight and clear evidence for the grafting of thiol ligands to MoS_2, X-ray photoelectron spectroscopy (XPS) was employed to characterize the MPA-MoS_2 sample (Figure 1b). The XPS analysis revealed distinctive peaks at binding energies of 288.6 eV and 286.2 eV, each corresponding to the C-O and C=O functional groups, which provides clear evidence of the successful attachment of MPA onto the exfoliated MoS_2 nanosheets. Moreover, our analysis revealed a significant shift towards higher binding energies in both the Mo and S peaks of MoS_2 upon functionalization (Figure S1). This observed shift can be attributed to the electron-withdrawing nature of the attached -COOH groups of MPA which possess electronegative oxygen atoms, which have a stronger affinity for electrons compared to the Mo and S atoms in MoS_2.[30]

The MPA-MoS_2 dispersion (Figure 1c) was further analyzed with transmission electron microscopy (TEM). As presented in Figure 1d, few-to-monolayer MPA-MoS_2 nanosheets show wrinkled sheets that are partially folded. The scanning electron microscopy (SEM) image of the MPA-MoS_2 deposited on Si wafer clearly shows 2D nanoflakes with basal plane and edges (Figure S2). With Lambert-Beer Law, the estimated concentration of MoS_2 nanosheets/dimethylformamide (DMF) dispersion is ≈ 0.8 mg/mL. The optical absorption spectrum of the dispersion (Figure 1e) reveals the peak located around 670 nm and a broad band at around 400 nm with a shoulder at 350 nm. The peak at 670 nm can be assigned to the characteristics of a 2H-MoS_2 nanosheet, which is in good agreement with MoS_2 thin layers obtained from a liquid-based exfoliation method.[31] Furthermore, the optical band gap of the MPA-MoS_2 nanosheets in dispersion was found to be ≈1.8 eV (the inset to Figure 1e).

Before introducing the MoS_2 nanosheets directly into the perovskite precursor, we analyzed how the MPA ligand influences the uniformity and stability of the prepared MoS_2 colloidal dispersion. The literature reports that exfoliated 2D nanosheets without surfactants tend to restack easily[23], which limits reproducibility when used as an additive. As shown in Figure S3, we compared the appearance of freshly prepared dispersions with those that had been left to stand for one day. It is evident that, after only one day, the MoS_2 dispersion without the MPA ligand had almost completely precipitated to the bottom. In contrast, the MPA-MoS_2 dispersion remained clear and uniform, due to the MPA ligand preventing complete restacking. The importance of a stable colloidal dispersion is crucial, as it directly influences the results when the dispersion is added to the perovskite precursor. If the 2D nanosheets restack easily, it will adversely affect the reproducibility of the result. Ensuring that the dispersion remains stable and well-dispersed is essential for achieving consistent and reliable results.

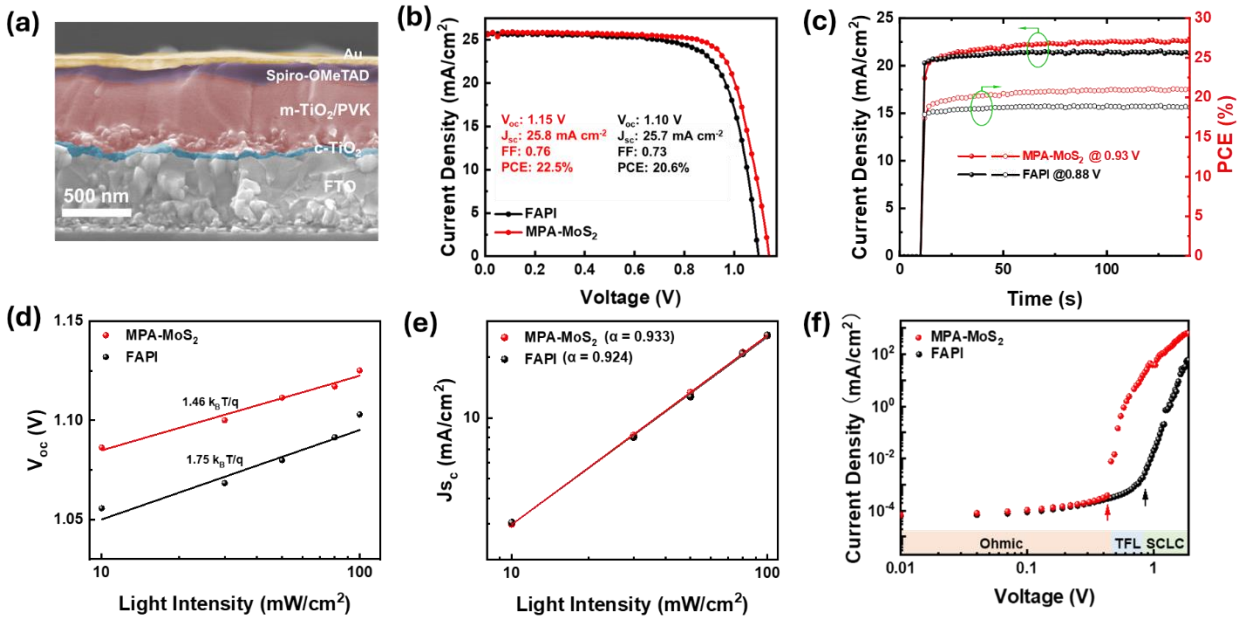

Figure 2. a) cross-section SEM of perovskite device. b) Current density–voltage (J–V) curves (reverse scan) of the champion PSCs based on FAPI films with and without MPA-MoS_2. c) Steady-state PCE and Jsc of the corresponding devices measured at the maximum power point. Dependence of d) Voc and e) Jsc at various illumination intensities. f) Current density–voltage curves of electron-only device (FTO/bl-TiO_2/PVK/PCBM/BCP/Ag)

We have fabricated the control and MPA-MoS_2 incorporated FAPI PSCs with a p-i-n device architecture of fluorine-doped tin oxide (FTO)/bl-TiO_2/perovskite/Spiro-OMeTAD (2,2',7,7'-Tetrakis[N,N-di(4-methoxyphenyl)amino]-9,9'-spirobifluorene)/Au to evaluate the influence of the 2D additives on the photovoltaic performance (Figure 2a). After adding the MPA-MoS_2 dispersion into the precursor, it is noteworthy that the solution maintains its clarity, suggesting a stable mixture system conducive to subsequent deposition process. The MPA-MoS_2 dispersion concentration of 0.1 mg/mL was used as the optimal condition for maximizing the device performance enhancement (Figure S4 and Table S1). The measured PSC for MPA-MoS_2 modified PSCs clearly display a statistically significant, large improvement compared to the control FAPI PSC without the 2D additive (Figure 2b, S5, and S6), largely driven by pronounced enhancement in open-circuit voltage (V_{oc}) and fill factor (FF), and mild increase in short circuit current density (J_{sc}). Steady-state photocurrent and power output have been evaluated by maximum power point tracking (Figure 2c), with PCE of MPA-MoS_2 incorporated device stabilizing at 22.0 % as opposed to 21.0 % in the device with pure MoS_2 and 20.0 % in the control device. The champion FAPI/MPA-MoS_2 device achieved PCE of 22.5%, where the simultaneous improvements in V_{oc} (1.15 V), J_{sc} (25.8 mA cm^{-2}), and FF (0.76) are observed. Meanwhile, the best performing pristine MoS_2-based (no MPA functionalization) device delivers a lower PCE of 21.3 % with V_{oc} of 1.13 V, J_{sc} of 25.8 mA cm^{-2}, and FF of 0.73, whereas the control PSC without any additive yields the lowest PCE of 20.6%. The corresponding photovoltaic performance parameters are listed in the in-set tables of Figure 2b. As shown in Figure S7, the external quantum efficiency (EQE) spectra of the champion device based on MPA-MoS_2 displayed an integrated J_{sc} well matching J_{sc} from J-V scan. We also prepared a pure MoS_2-added FAPI device, which showed slightly higher efficiency than the control. However, its performance was still lower than that of the MPA-MoS_2 device as shown in Figure S5 and S8.

To elucidate the origin of the enhanced device performance with MPA-MoS_2, we investigated the dependence of V_{oc} and J_{sc} on illumination intensity to probe charge recombination characteristics. Figure 2g illustrates the dependence of V_{oc} on light intensity for PSCs. Generally, a slope of kT/q (with k being Boltzmann constant, T temperature, and q elementary charge) indicates the dominance of radiative recombination, while a slope of 2 × kT/q the non-radiative, Shockley-Read-Hall recombination.[32] The slope of control device was found to be 1.75 kT/q, whereas those of FAPI/MPA-MoS_2 devices were 1.46, respectively,

suggesting a reduced non-radiative recombination, which is typically medicated via defect states, under the tested open-circuit condition. Figure 2h presents the plots of J_{sc} versus illumination intensity, with the exponential factor α assessing the degree of bimolecular recombination in the PSCs (which typically occurs at junctions). The MPA-MoS_2 incorporated device features an exponential factor α closer to 1 (unity) compared to the pure FAPI device, implying that the perovskite film optimized by MPA-MoS_2 additive could effectively enhance charge drift and reduce the interfacial recombination under the short-circuit condition.

Additionally, we investigated the charge transport behavior of each perovskite layer using the space charge-limited current method based on electron-only devices (FTO/bl-TiO_2/perovskite/phenyl-C_{61}-butyric acid methyl ester (PCBM)/ bathocuproine (BCP)/Ag). As shown in Figure 2i, the calculated electron mobility of FAPI/MPA-MoS_2 (4.24×10^{-2} cm^2 V^{-1} s^{-1}) was considerably improved in comparison to that of the control FAPI without the additives (1.50×10^{-2} cm^2 V^{-1} s^{-1}). The enhanced electron mobility can contribute to the efficient extraction of photogenerated charge carriers from the FAPI layer, as well as to the reduction of charge carrier recombination at the interface. Moreover, we quantitatively estimated the trap density using the data and found that the FAPI/MPA-MoS_2 had a much lower trap density, 1.49×10^{15} cm^{-3}, compared to the control FAPI (9.155×10^{16} cm^{-3}), illustrating that the incorporation of MPA-MoS_2 is beneficial to passivating defect states.

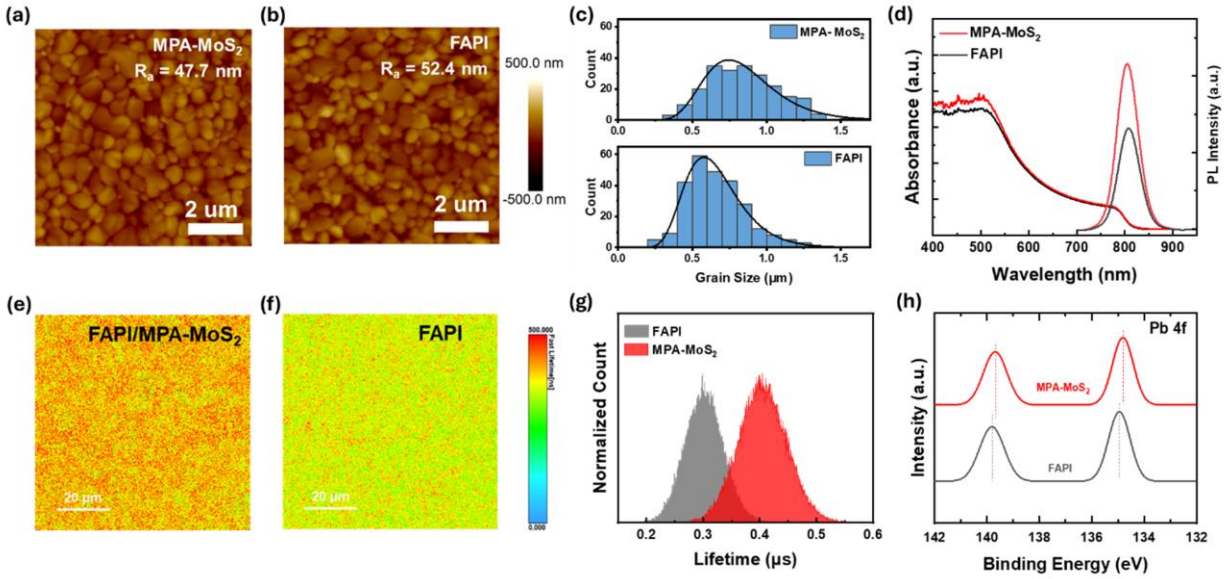

Figure 3. AFM images of a) FAPI/MPA-MoS_2 film and b) FAPI film. c) Statistical analysis of perovskite film grain sizes from AFM images. d) Optical absorption and PL spectra of FAPI films with and without MPA-MoS_2. e) and f) PL mapping of FAPI films with and without MPA-MoS_2 and g) the corresponding lifetime distribution. h) XPS spectra of Pb 4f from FAPI films without and with MPA-MoS_2.

To comprehensively understand the impact of MPA-MoS_2 additives on the crystal structure, film morphology, and optical properties of FAPI films, an array of complementary materials characterizations were carried out on the perovskite films. Previous research has demonstrated that MoS_2 can passivate grain boundary defects and enhance the film quality.[33, 34] First, atomic force microscopy (AFM) and SEM revealed the surface morphology of the FAPI film with and without MPA-MoS_2. Figure 3a-c displays the AFM micrographs and the corresponding grain size distribution of the perovskite films. It is found that the FAPI/MPA-MoS_2 shows a smoother surface with a reduced root-mean-square roughness of 47.7 nm, compared to 52.4 nm of pure FAPI film or 51.1 nm of FAPI with unmodified MoS_2 (Figure S12a). The average grain size of FAPI also increased to ~850 nm with the addition of MPA-MoS_2, whereas the pure FAPI film or FAPI with unmodified MoS_2 (Figure S12b) show an average grainsize of ~600 nm, again suggesting important roles of MPA ligands in enhancing the overall properties of the FAPI film, including crystallization and grain growth in this case. Top-view SEM images are shown in Figure S9, the FAPI/MPA-MoS_2 film demonstrates a more uniform, regular morphology as compared to the pure FAPI. The X-ray diffraction (XRD) patterns of both the control and MoS_2-incorporated FAPI films featured prominent peaks at 13.9° and 28.1°, corresponding to the (100) plane and (200) of a cubic α-FAPI phase .[35] The unaltered peak positions indicate that MoS_2 nanosheets, regardless of whether they are functionalized or not, are not directly embedded within the perovskite crystal lattice, thus not influencing the FAPI lattice constant (Figure S10). Meanwhile, the increased intensity of the characteristic diffraction peaks upon the addition of MoS_2 suggests the enhanced crystallinity, which is consistent with the result from the previous study, where the addition of MPA-MoS_2 in the perovskite precursor could help trigger the heterogenous nucleation to induce the crystallization process during the annealing process.[34, 36]

The effects of MPA-MoS_2 nanosheets on the charge carrier dynamics in the FAPI films were then studied by the steady-state photoluminescence (PL) and the time-resolved PL (TRPL) experiments. In Figure 3d and Figure S12c, the optical absorption spectrum of the FAPI films

with MPA-MoS_2 or unmodified MoS_2 is almost identical to that of the pristine FAPI thin film (identical thicknesses), indicating no significant change in the absorption in the visible wavelength range by the added MoS_2. However, under the same excitation intensity, the FAPI thin film with MPA-MoS_2 exhibited the strongest PL emission intensity relative to the pure FAPI and FAPI/MoS_2 films. The stronger PL emission is likely attributed to the effective passivation of non-radiative recombination centers at the grain boundaries by MPA and reduced surface defects provided by the increased grain size.[14] The TRPL spectra (Figure S11) are fitted using the bi-exponential decay model, and the results are summarized in Table S2. The FAPI/MPA-MoS_2 film exhibits the highest average PL lifetime of 248.5 ns, compared to those of the pristine FAPI (82.6 ns) and FAPI/MoS_2 (179.0 ns). The prolonged PL lifetime further confirmed the improved charge carrier transport and reduced non-radiative recombination losses in the FAPI film with MPA-MoS_2.

To probe the spatial distribution of defect states, PL mapping was further performed, examining the control and MPA-MoS_2-modified FAPI films (Figure 3e-g). Compared with the pure FAPI film, both FAPI/MPA-MoS_2 and FAPI/MoS_2 (Figure S12d and e) show enhanced PL lifetime, indicating the effective defect passivation by MoS_2, but, especially with MPA modification given its most enhanced lifetime. Furthermore, the lifetime of the MoS_2-modified samples presents relatively more uniform spatial distribution (Figure 3g and Figure S12d), suggesting the nanosheets are uniformly incorporated and passivating the perovskite films. FAPI/MPA-MoS_2 film exhibits the longest lifetime in comparison to the pristine FAPI, again indicating the contribution of MPA in reducing non-radiative recombination.

The chemical interaction between the FAPI perovskite films and MPA-MoS_2 were investigated by XPS measurements. In Figure 3h, the high-resolution Pb 4f spectrum exhibits two characteristic peaks attributed to $4f_{5/2}$ and $4f_{7/2}$ of divalent Pb^{2+} located at 143.1 and 138.3 eV, respectively, for the pristine FAPI film. For the film with MPA-MoS_2, these two peaks are shifted to lower binding energies (142.9 and 138.1 eV). The same red shift was also observed in the I 3d spectra (Figure S13). We attribute these shifts to the chemical interaction of the carboxyl group of MPA-MoS_2 with FAPI, particularly its uncoordinated Pb and I ions, leading to their passivation.

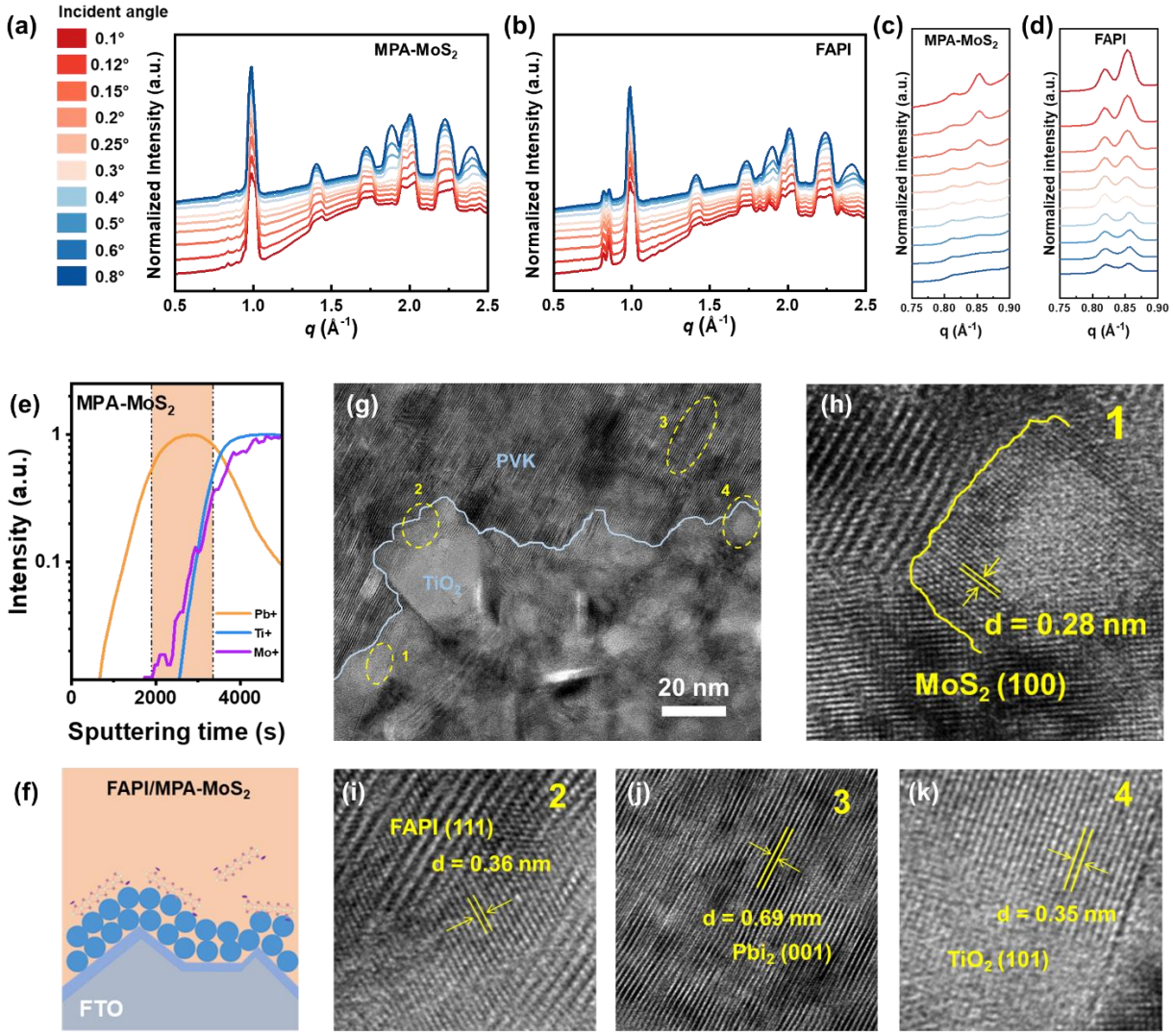

Figure 4. a, b) ex-situ GIWAXS intensity profiles for the FAPI films with or without MPA-MoS2 under different incident angles and c, d) magnified region of ex-situ GIWAXS intensity profiles focusing on 0.75° to 0.9° with normalized Intensities. e) ToF-SIMS depth profiles of FAPI/MPA-MoS2. f) Schematic diagram of the proposed regions of MPA-MoS2 distributed within FAPI perovskite films; g) Cross-sectional HRTEM images near the boundary region between bl-TiO2 and FAPI/MPA-MoS2 layers; h-k) Magnified HRTEM images of the yellow circled area.

While surface structural characterizations provide valuable information on the quality of FAPI films with MoS_2 in general, gaining a comprehensive understanding requires a deeper exploration of the internal structure. To achieve this, we conducted synchrotron-based depth-resolved GIWAXS measurements, allowing us to probe the presence of non-photoactive δ-FAPI

phase at specific depths by varying the incident angle.[37] We selected a range of incident angles, ranging from 0.1° to 0.8°, to specifically target different depths within the film during the GIWAXS analysis. These angles were chosen to examine the structural characteristics of the top surface, the middle layer, and the entire film structure (Figure 4a and 4b). In Figure 4c and 4d, we present the radially integrated GIWAXS patterns covering a q range from 0.75 $Å^{-1}$ to 0.9 $Å^{-1}$, corresponding to the region associated with the characteristic scattering features of δ-FAPI. The vertical axis represents the normalized scattering intensity with respect to the intensity of (100) plane of photoactive cubic α-FAPI (denoted as $\alpha(100)_c$). The control FAPI film exhibits two prominent peaks throughout the entire film, observed at approximately 0.83 $Å^{-1}$ and 0.86 $Å^{-1}$, which correspond to (100) and (101) planes of non-photoactive, hexagonal δ-phases (denoted as $\delta 2H(100)_h$ and $\delta 6H(101)_h$).[38] In comparison, MPA-MoS_2 samples exhibit lower δ-FAPI intensity, hinting at the notion that MoS_2 nanosheets improve the formation of photoactive α-phase. Interestingly, we also observed that the normalized intensity of δ-FAPI is relatively higher at smaller incident angles compared to larger angles, suggesting a varying distribution of this non-photoactive phase along the film thickness, specifically more near the surface. Furthermore, from the integrated GIWAXS spectra with a q range from 0.5 $Å^{-1}$ to 2.5 $Å^{-1}$, the presence of TiO_2 signal is detected at incident angles larger than 0.3°, indicating the detection of the bottom interface between the perovskite and TiO_2 layers. For the pure MoS_2 system, while we observed a similar trend with a lower fraction of δ-FAPI at the bottom of the film (Figure S14), compared to the MPA-MoS_2 system under the same incident angle, we found that the fraction of δ-FAPI is higher in the pure MoS_2 film. Overall, the GIWAXS results indicate that the presence of MPA-MoS_2 in the FAPI film leads to: (1) overall, a higher fraction of α-FAPI phase within the FAPI film and (2) an increased fraction of α-FAPI as getting closer to the bottom layer, which allude to a potential role of MPA-MoS_2 in templating the formation of the α-FAPI phase from the bottom side of the FAPI film.

It is noted that all the presented complementary electrical, optical, and structural characterization data confirm that the incorporation of MPA-MoS_2 improved the electrical properties of FAPI films, including increased charge mobility and reduced charge trap density and associated non-radiative recombination, which can be attributed to the two combined factors, namely, the passivation of grain boundaries and the stabilization of favorable α-phase FAPI. It is

however challenging to quantitatively distinguish the relative contributions from these two factors. Given the large grain boundary density and the observed chemical interaction between FAPI and MPA, we expect the grain boundary passivation by MPA-MoS_2 might be a more dominant factor. In the meantime, one can also speculate the role of MPA itself as an additive considering prior studies showing that small molecules having a similar structure as MPA with bifunctional groups could interact strongly with polar molecules and metal cations (e.g., dimethyl sulfoxide (DMSO) and $[PbI_6]^{4-}$), thus being able to suppress the rapid reaction of perovskite precursors, stabilizing the solution when used as additives.[39] However, such a scenario would require the addition of a large amount of freely mobile additive molecules in the perovskite solution, unlike the current study where the small amount of added MoS_2 renders the amount of incorporated MPA even smaller because MPA molecules are only bound to MoS_2 surface likely with incomplete coverage to only improve the colloidal stability of the MoS_2 dispersion itself. Therefore, we expect the direct influence of MPA molecules themselves on the FAPI crystallization is negligible compared with that of MoS_2.

In order to further understand the underlying mechanisms and interactions between MPA-MoS_2 and FAPI, we utilized ToF-SIMS to directly determine how the attached thiol ligand affects the presence of added MPA-MoS_2 nanosheets within FAPI films. The ToF-SIMS compositional depth-profiling was performed on FAPI/MPA-MoS_2 films to probe the distribution of the incorporated nanosheets across the FAPI film. The perovskite films were deposited onto bl-TiO_2/FTO substrates to replicate the bottom interface in actual PSCs. Additionally, to facilitate the clear identification of the top interface of the perovskite films, a thin layer of deuterated polystyrene (d-PS) was coated on top of the perovskite films. As shown in Figure 4b and 4c, the normalized ToF-SIMS depth profiles show the relative intensities for Pb^+, Mo^+, and Ti^+ ions versus sputtering time, where each ion represent the FAPI film, added MoS_2 and TiO_2 layer, respectively. The highlighted orange region in the depth-profile represents the approximate region corresponding to the FAPI films. It is important to note that the sputtering time presented in the depth profiles may not directly correspond to the actual film thickness due to variations in sputtering rates caused by differences in chemical composition between each layer. The distribution of MPA-MoS_2 within the perovskite film is concentrated mostly in the bottom region. Particularly, the Mo^+ curve displays a similar rising profile to that of Ti^+, indicating that MPA-MoS_2 is primarily concentrated within the FAPI/bl-TiO_2 interfacial

region as shown in Figure 4c. The accumulation of MPA-MoS_2 at the perovskite/bl-TiO_2 interface suggests its potentially beneficial impact on the electron extraction efficiency of PSCs by suppressing carrier recombination at the bottom interface. This notion of an efficient electron extraction from the FAPI layer by MoS_2 accumulated near the bottom interface is consistent with the results obtained from electron-only devices (Figure 2i), in which the addition of MPA-MoS_2 in FAPI increased the apparent electron mobility due to an improved charge extraction.

To provide a more direct characterization of the MoS_2-MPA within the FAPI film, we employed cross-sectional high-resolution TEM (HRTEM) and probed the presence of MPA-MoS_2 at the FAPI/bl-TiO_2 interface region. In the cross-sectional HRTEM image of FAPI/MPA-MoS_2 film (Figure 4g-k), the approximate location of the interface between FAPI and bl-TiO_2 is marked by the blue line. This determination was made based on the observed change of lattice spacing. The TiO_2 nanoparticles within bl-TiO_2 layer are clearly identified by the presence of atomic lattice fringes measuring approximately 0.35 nm (Figure 4k), which corresponds to the (101) crystal plane of TiO_2. The FAPI perovskite crystal displays atomic lattice fringes of 0.36 nm (Figure 4i), which corresponds to the (111) crystal plane of α-FAPI.[38] Also observed is a large area exhibiting wider lattice fringes with an interspacing of approximately 0.68 nm (Figure 4j), which corresponds to PbI_2.[40] The presence of PbI_2 is likely caused by the degradation of FAPI during the TEM sample preparation using focused ion beam (FIB). Notably, a distinctive and brighter region is observed at the interface between the FAPI perovskite and bl-TiO_2 regions in the HRTEM image (Figure 4h). Within this region, well-defined lattice fringes are clearly visible, exhibiting a spacing of 0.28 nm. This observed lattice spacing matches the reported interplanar spacing of the (100) plane for MoS_2.[41] Meanwhile, it is noted that the elemental mapping by energy dispersive spectroscopy (EDS) didn't yield detectable signal of MoS_2 (Figure S15), which is attributable to the relatively low concentration of MPA-MoS_2 incorporated into the FAPI films below the detection limit of EDS. The findings from both HRTEM and ToF-SIMS characterizations provide a strong support for the notion that the MPA-MoS_2 nanosheets are predominantly situated in the lower portion of the perovskite films, particularly near the TiO_2 interface. This localization suggests that the thiol ligand of MPA-MoS_2 may enhance the adhesion of MoS_2 to the bl-TiO_2 layer surface.

To understand the role of MPA-MoS_2 in promoting α-FAPI formation, in-situ GIWAXS measurements were conducted, monitoring the perovskite crystallization dynamics during thermal annealing. After the precursor solution was spin-coated onto a glass substrate, the sample was immediately transferred to a hot stage that was integrated at the synchrotron X-ray beamline, which was identical to that used in our previous study.[42] Subsequently, the as-cast sample was heated from room temperature to 150 °C, with a ramp rate of 30 °C/min, under an N_2 atmosphere and a relative humidity (RH) ~10%. The continuous N_2 atmosphere and controlled moisture level were maintained during the thermal annealing process to best emulate the actual processing conditions for perovskite films. During this heating cycle, 2D GIWAXS patterns with azimuthal angle from 0° (vertical axis) to 90° (horizontal axis) were collected every second (Figure 5a-f).

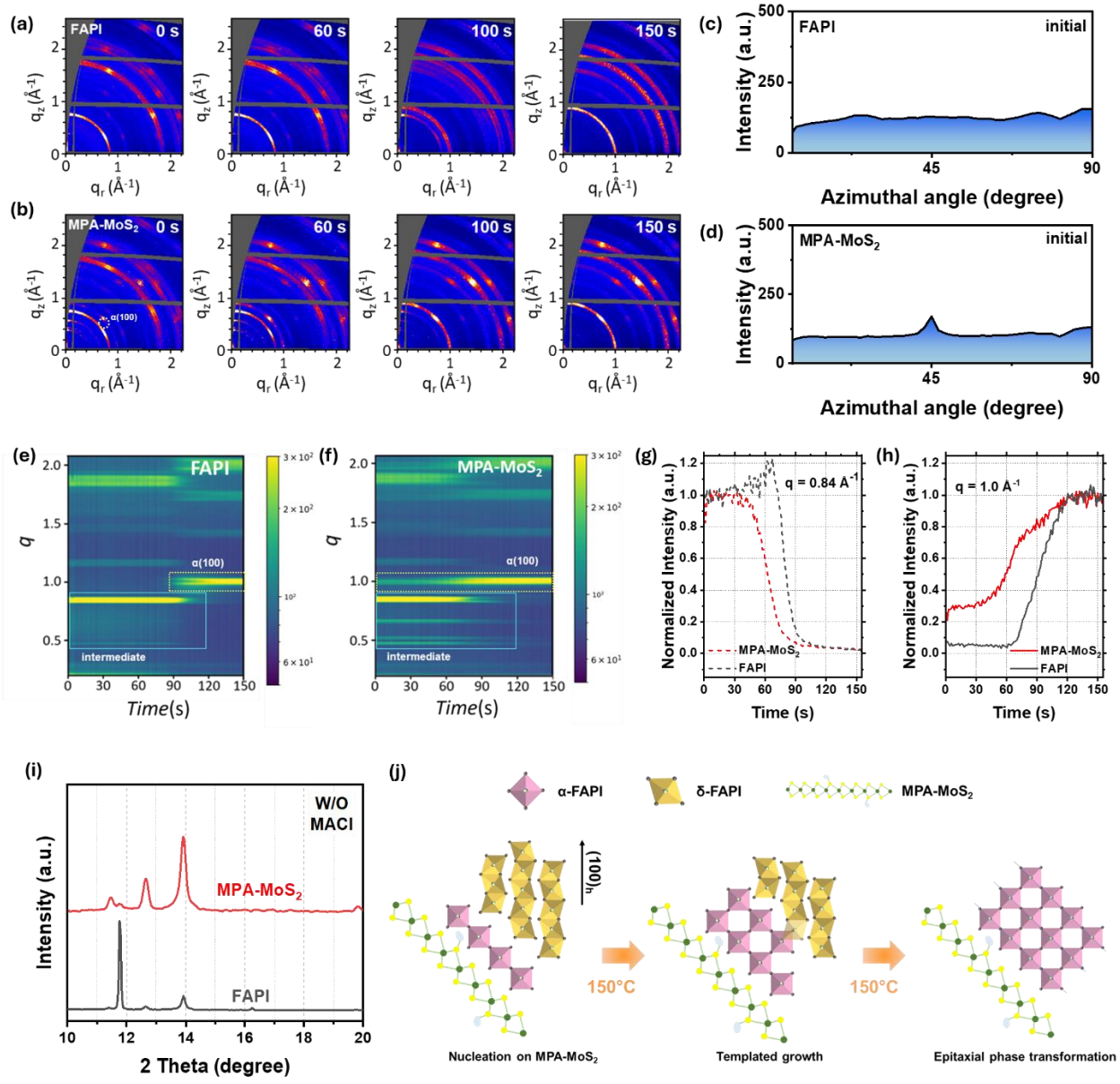

Figure 5. a, b) 2D in-situ GIWAXS scattering patterns from FAPI perovskite films (FAPI and FAPI/MPA-MoS_2) during thermal annealing. c, d) The plots of scattering intensity integrated azimuthally at q = 1.0 $Å^{-1}$ ($\alpha(100)_c$) for 0 s annealing. e, f) The radially integrated GIWAXS intensity (from 2D GIWAXS patterns obtained at different time) plotted as a function of q and time. g, h) Temporal evolution of the scattering intensities corresponding to the intermediate (q = 0.84 $Å^{-1}$) and α-FAPI phase (q = 1.0 $Å^{-1}$) as a function of annealing time. i) XRD spectra of FAPI films prepared without MACl. j) A schematic illustration of the roles of the 2D MPA-MoS_2 in templating the nucleation and growth of α-FAPI.

Notably, the diffraction peak (ring) at approximately 0.84 $Å^{-1}$ at the beginning of the annealing cycle (time = 0 s) corresponds to the non-photoactive $\delta 2H(100)_h$ phase of FAPI (i.e., intermediate phase) (Figure 5a,b), while additional peaks around q = 0.4 and 0.58 $Å^{-1}$ is likely resulting from residual solvent molecules. As the annealing time increases, the diffraction peak from the intermediate phases gradually diminishes due to the rapid desorption of volatile MACl and the removal of residual solvent molecules. Simultaneously, with increasing annealing time, the intensity of the ring at around q = 1.0 $Å^{-1}$ steadily amplifies (Figure 5a,b), which originates from (100) plane of photoactive α-phase FAPI ($\alpha(100)_c$).[43] Overall, these observations indicate a progressive conversion of the intermediate hexagonal δ-FAPI to the final α-FAPI under thermal annealing. Interestingly, unlike the pure FAPI film, the MPA-MoS_2 incorporated FAPI features a presence of photoactive α-phase even without annealing at the initial stage—an $\alpha(100)_c$ diffraction spot is clearly visible at q = 1.0 $Å^{-1}$ and azimuthal angle ~45° in the 2D scattering pattern (Figure 5b, time = 0 s), which suggests MPA-MoS_2 additive induces the formation of α-phase structure upon spin-coating. The fact that the $\alpha(100)_c$ diffraction spot appears at a particular azimuthal angle (~45°), as re-confirmed in the scattering intensity versus azimuthal angle plot at q = 1.0 $Å^{-1}$ (Figure 5c,d), indicates the crystallization of a-phase in the FAPI/MPA-MoS_2 sample occurs with a preferred orientation, supporting the possibility that MPA-MoS_2 nanosheets template the FAPI crystallization. Meanwhile, the MPA-MoS_2 incorporated FAPI sample maintains a strong $\alpha(100)_c$ diffraction intensity at 45° even after annealing as shown in Figure S16.

The effects of MPA-MoS_2 on the annealing-time-dependent crystallization dynamics of α-FAPI phase is more quantitatively analyzed by visualizing the radially integrated scattering intensity versus q plots (from 2D GIWAXS patterns) with respect to annealing time (Figure 5e,f). The plots clearly show the existence of α-phase in the FAPI/MPA-MoS_2 sample before annealing ($\alpha(100)_c$ diffraction around q = 1.0 $Å^{-1}$) and an intensified crystallization (i.e., increasing $\alpha(100)_c$ intensity) with increasing annealing time (Figure 5f), in contrast to the pure FAPI that features $\alpha(100)_c$ diffraction peak that only appears later in the annealing time (Figure 5e). Also apparent is an earlier disappearance of δ-phase peak (q = 0.84 $Å^{-1}$) in FAPI/MPA-MoS_2 compared to the control pure FAPI.

By monitoring the evolution of diffraction peaks corresponding to the photoactive α-phase (q = 1.0 $Å^{-1}$) and intermediate δ-phase (q = 0.84 $Å^{-1}$) with annealing time, the perovskite

phase conversion can be broken down into two stages (Figure 5g,h). During stage I, the intensity of the δ-phase remains stable (Figure 5h) as the system requires additional thermal energy to initiate its phase conversion to α-FAPI. Once sufficient thermal energy is absorbed, the system enters stage II, and the δ-phase begins to convert to the α-phase (Figure 5h). In the pristine FAPI system, the intensity of the intermediate δ-phase showed a continued increase during the initial stage of annealing and peaked at ~60 s, unlike FAPI/MPA-MoS_2 that shows a steady δ-FAPI intensity until ~30 s, which is followed by a rapid decrease in its intensity (Figure 5h). The initial increase of δ-phase in the pure FAPI system during the annealing is most likely due to the incomplete, MACl-assisted δ-FAPI nucleation process occurring during spin-casting. In contrast, the steady intensity of the δ-phase during the early stage of annealing in the FAPI/MPA-MoS_2 system indicates a complete nucleation of the intermediate δ-phase upon spin-coating. Consistent to the noted evolution of the δ-phase during annealing, the appearance of photoactive α-phase starts ~30 s earlier in the FAPI/MPA-MoS_2 system than in the pure FAPI system (Figure 5h). Overall, all the presented GIWAXS data unambiguously confirm that the presence of MPA-MoS_2 clearly facilitates the initiation of the δ-to-α phase conversion process in FAPI during the annealing.

To further investigate the influence of MPA-MoS_2 on the phase formation in the FAPI film, an additional experiment was conducted without the presence of MACl as depicted in Figure 5i. In the pure FAPI system, the predominant phase observed was δ-FAPI even after annealing, in line with previous reports.[44] However, in the FAPI/MPA-MoS_2 system, there was a remarkable enhancement in the formation of the α-FAPI phase despite the absence of MACl. This again strongly supports the notion that the MPA-MoS_2 additive enhances the crystallization and phase transition process towards the photoactive α-phase. Based on these experimental observations, we propose that the 2D MPA-MoS_2 nanosheet serves as a template for FAPI phase conversion (Figure 5j), which are known to be driven by entropy contribution from the change in the organic FA cation's rotational modes.[45] Initially, the 2D nature of MPA-MoS_2 nanosheets offers a large surface area, facilitating the adsorption and assembly of perovskite precursors. The strong affinity between the Pb^{2+} ions in the perovskite and the MPA-MoS_2 nanosheets, enabled via the C=O interaction, promotes the preferential adsorption of $[PbI_6]^{4-}$ clusters onto the MPA-MoS_2 nanosheets. These clusters should act as building blocks and nucleation sites for the

subsequent growth of perovskite crystals, considering that 2D nanosheets, such as MoS_2, are known to have in-plane coupling with perovskite crystals due to commensurate lattice constant, providing an ideal template for the perovskite's epitaxial growth.[46, 47] In turn, the perovskite phase existing in the as-cast state can enhance a lateral perovskite crystal growth, resulting in a reduced grain boundary density.[48]

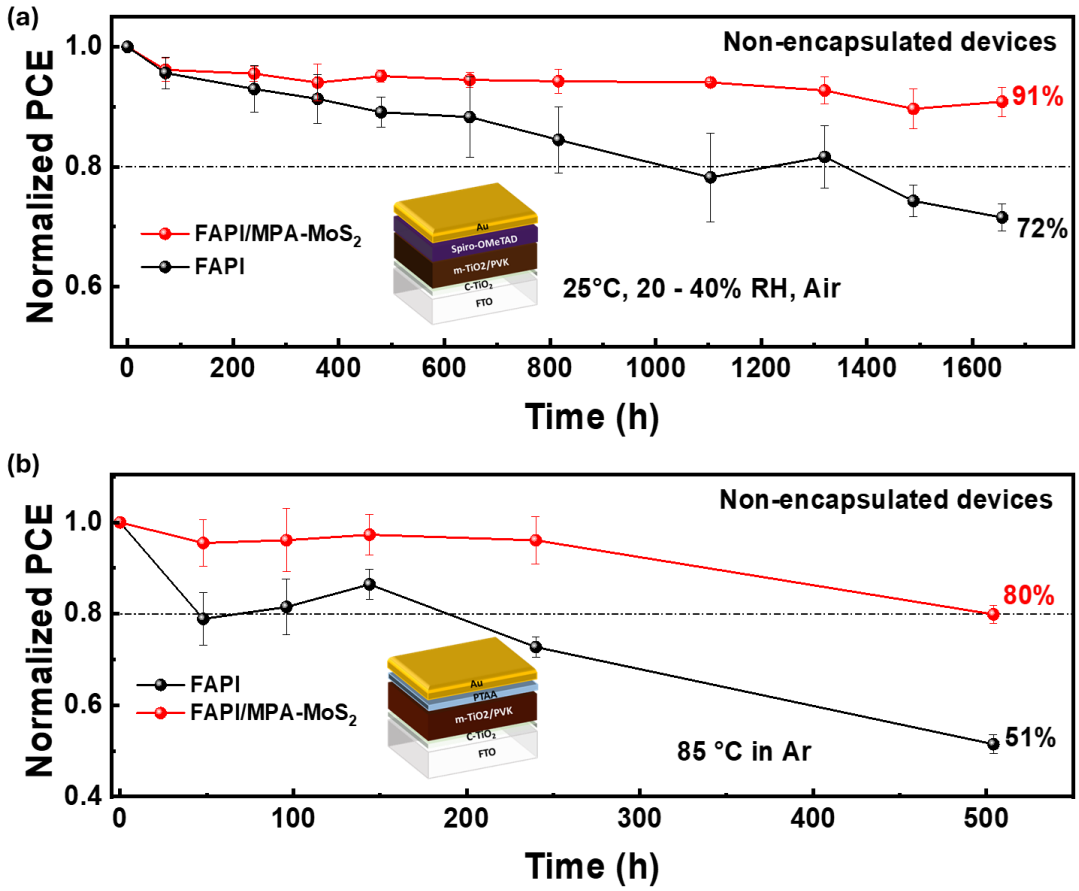

Figure 6. Time-dependent evolution of PCE in non-encapsulated PSCs (FAPI and FAPI/MPA-MoS_2) under a) ambience, b) heating at 85 °C in Ar.

We investigated the effects of the MPA-MoS_2 nanosheet additive on the long-term stability of the FAPI PSCs under various environmental stresses. Initially, the effects on the conventional n-i-p architecture using Spiro-OMeTAD hole transfer layer (HTL) were examined.

The devices underwent a shelf test in ambient conditions at 25 °C and 20-40% RH for over 1600 hours (Figure 6a). Notably, the control FAPI device without MPA-MoS_2 experienced a reduction in PCE to 72% of the starting value, while the PCE of the FAPI/MoS_2 device stabilized at 81% (Figure S19). In contrast, the PCE of the FAPI/MPA-MoS_2 device maintained 91% of its original value. These results indicate the presence of the MPA-MoS_2 additive significantly retards the degradation of FAPI. Considering that Spiro-OMeTAD—an HTL used in the current study—is thermally unstable, we also conducted additional tests using a more stable PTAA (poly [bis (4-phenyl) (2,4,6-trimethylphenyl)amine]) as an HTL to analyze the impact of our strategy on thermal stability. The PSCs with the device structure comprising FTO/bl-TiO_2/perovskite/PTAA/Au were employed for this purpose (Figure 6b). The J-V curves and photovoltaic parameters of these devices were presented in Figure S17 and Table S3. The unencapsulated PSCs were subjected to thermal stress at 85 °C on a hot plate under a dark, Ar atmosphere. After more than 500 hours of annealing, the average PCE of the MPA-MoS_2 incorporated FAPI device maintained 80% of its initial value, whereas the FAPI/MoS_2 device retained only 68% of its initial PCE, and the control FAPI 51%. Clearly, the thermal stability of the FAPI/MPA-MoS_2 device outperformed that of both the FAPI with bare MoS_2 and reference pure FAPI devices. This observed thermal stability in the FAPI/ MPA-MoS_2 originates from the reduced thermal degradation of FAPI crystal as supported by XRD data (Figure S18). Finally, we investigated the influence of the 2D MPA-MoS_2 additive on the stability of PCE under the open-circuit condition with continuous one-sun illumination in an Ar atmosphere (Figure S20). The PSC performance generally decays faster when exposed to the open-circuit condition than maximum power point. Also, the device stability under open circuit is practically important because it directly influences the field deployment of solar panels, and the panels will usually be exposed at open-circuit condition for a certain period before getting connected to the grid. We stressed our devices at this relatively harsh condition to emphasize the benefits of MoS_2 nanosheets: we observed that the control FAPI device maintained only 29% of its initial PCE after ~50 hr illumination, whereas the FAPI/MPA-MoS_2 device retained 57% of their initial PCE and the FAPI/MoS_2 device retained 47% after the same aging duration under illumination. Clearly, the open-circuit stability of FAPI/MPA-MoS_2 device is superior to that of the reference FAPI device, which we attribute to the reduced grain boundary density and, potentially,

passivation of grain boundaries, thus effectively blocking the migration and decomposition of organic components.

Conclusions

In this study, we successfully fabricated highly crystalline and oriented FAPI PSCs with enhanced photovoltaic efficiency and stability by utilizing the 2D MPA-MoS_2 nanosheet additive. The presence of MPA-MoS_2 near the bottom interface of FAPI layer with bl-TiO_2 was identified using ToF-SIMS, while HRTEM analysis directly confirmed the presence of crystalline MPA-MoS_2 nanosheets on the TiO_2 surface. As revealed by in-situ synchrotron GIWAXS data obtained during thermal annealing, the localized MPA-MoS_2 nanosheet on the TiO_2 surface served as a favorable template for the nucleation and growth of the FAPI crystalline phase and conversion to the photoactive α-phase. As a result, the fabricated FAPI/MPA-MoS_2 PSCs achieved a PCE up to 22.5%. Finally, the device also demonstrated a notably enhanced stability under thermal stress and simulated solar irradiation (i.e., open-circuit condition) compared to FAPI/MoS_2 and pure FAPI devices. The results highlight the potential of ligand-functionalized 2D nanosheets as a promising processing additive for improving perovskite crystallization and phase conversion to the photoactive α-FAPI phase in not only PSCs but also other FAPI-based optoelectronic devices.

Experimental Section

Materials

All the solvents and salts were used in their as-received condition without any further purification. DMF (anhydrous, 99.8%), DMSO (anhydrous, >99.9%), chlorobenzene (CB, anhydrous, 99.8%), 2-propanol (anhydrous, 99.5%), diethyl ether (anhydrous, ≥99.0%), 4-tert-butylpyridine (t-BP), acetonitrile, SHT-263 Solarpur, bis(trifluoromethylsulfonyl) imidelithium salt (Li-TFSI), FK209 Co(III) TFSI salt and MA chloride (MACl) were purchased from Sigma-Aldrich. Lead (II) iodide (PbI_2, 99.99%) was purchased from TCI. FA iodide (FAI, >99.5%), was purchase from Ossila.

Thiol Functionalization of Monolayer MoS_2

Monolayer MoS_2 was obtained from ACS Materials with a lateral size ranging mainly between 0.2 ~ 1 um. To ensure greater dispersion stability, the concentration of MoS_2 was controlled to 0.1 mg/ml. The powder was added into anhydrous isopropanol and sonicated using a tip sonicator for 30 min. The MoS_2 powder was mixed with anhydrous isopropanol and sonicated using a tip sonicator for 30 min. The ligand attachment and solvent exchange process were performed following a previously published method[23].

Specifically, 3-MPA was added to the MoS_2/IPA dispersion (at a ratio of 1:1 relative to the molecular weight of MoS_2) and stirred for 24 hours. The resulting dispersion was washed with anhydrous DMF using a centrifugation and redispersion process to eliminate any unbound ligands. The centrifugation process was conducted at 2000 rpm for 30 min, and this was repeated three times. The supernatant was then collected and its absorbance was measured using a ultraviolet (UV)-visible spectrophotometer.

Perovskite Precursor Solutions

1.35M perovskite precursors were prepared by dissolving 622.36 mg PbI_2 and 232.16 mg FAI in 1 ml mixed DMF and DMSO solution (800 μl DMF +200 μl DMSO), 35 mol% MACl was added to enhance the quality of perovskite films. In studies involving MPA-MoS_2, the additive was incorporated into the perovskite precursor via adding the prepared dispersion directly. We compared 0.05, 0.1 and 0.15 mg/ml, finding that 0.1 mg/ml is the optimal concentration for MPA-MoS_2.When comparing MoS_2 and MPA-MoS_2, we used a concentration of 0.1 mg/ml for both additives.

PSC and Electron-Only Device Fabrication

FTO substrates were sequentially washed with 2% Hellmanex cleaning solution, deionized (DI) water, and ethanol in an ultrasonic bath for 30 min, which was further treated with UV ozone 10 min prior to use. The TiO_2 film was spin-coated solution at 2000 rpm for 30 s, followed by sintering at 450 °C for 2 h. The precursor solution of compact-TiO_2 (c-TiO_2) was prepared following a literature procedure [49]. The mesoporous TiO_2 (m-TiO_2) layer was spin-

casted on top of c-TiO_2 with TiO_2 paste mixed in ethanol (1:6.5 mass ratio) at 4500 rpm for 10 min (spin speed ramp rate of 3000 rpm/s), followed by sintering at 500 °C for 20 min, completing bl-TiO_2.

The perovskite precursor was spin-coated onto FTO/c-TiO_2/m-TiO_2 with two-step program: 1,000 and 5,000 rpm for 10 and 30 s, respectively. During the second step, 150 μL of diethyl ether was drop-coated to treat the perovskite films. The substrate was dried on a hot plate at 150 °C for 10 min to produce FAPI halide perovskite thin film in an Ar-filled glovebox. For 2D surface passivation, the 10M ammonium iodide butyrate (BAI) solution was dissolved in IPA and spin-coated onto the perovskite surface at a 3000 rpm for 30s. The as-cast film was annealed at 80 °C for 10 min. The HTL was deposited by preparing a SHT-263 Solarpur solution (80 mg/ml in CB) and mixing it with 30 μL t-BP, 20 μL Li-TFSI (500 mg/ml in acetonitrile), and 30 μL FK 209 Co (III) TFSI (300 mg/ml in acetonitrile). The HTL was spin-coated onto the perovskite films at 4000 rpm for 30 s. Finally, Au electrodes (80 nm thick) were deposited via electron-beam evaporation with deposition rate of 0.1 Å/s for the first 10 nm and 1 Å /s for the rest. For electron-only devices, the top electrode was prepared by spin-casting PCBM (20 mg/ml PCBM solution spin-coated at 1500 rpm for 30 s followed by annealing at 90°C for 10 min) and BCP (0.5 mg/ml BCP solution spin-coated at 4000 rpm for 30 s, followed by annealing at 70°C for 10 min), and depositing a 100nm thick Ag electrode by thermal evaporation.

Photovoltaic Performance Measurements

The J-V characteristics of fabricated PSCs were measured by a modified probe station equipped with a 150 W solar simulator (Oriel, USA) with AM1.5G filter and precision semiconductor parameter analyzer (Agilent). The light intensity was calibrated to 100 $mWcm^{-2}$ (1 Sun) by a calibrated Si solar cell (Oriel) before each measurement. The device active area was defined by the top circular Au electrode with 0.2 cm diameter. The J-V scan rate was 100 $mV \cdot s^{-1}$ in both reverse and forward scans. EQE measurements were conducted using a home built EQE set-up comprising a 300 W xenon lamp (Oriel) and monochromator (Oriel), attached to the probe station. All the photovoltaic measurements were performed in ambient air.

In-Situ GIWAXS Measurements

The in-situ GIWAXS data during thermal annealing were collected at the Complex Materials Scattering (11-BM) beamline of the National Synchrotron Light Source II at Brookhaven National Laboratory. To prepare a sample, FAPI precursor solution was spin-cast on an FTO glass/c-TiO_2/m-TiO_2 (from bottom to top in sequence) substrate, and the as-cast sample were immediately transferred to the beamline without any prior thermal annealing. The sample was mounted on a heating stage integrated to the beamline, and during the measurement, the sample was heated from room temperature to 100 °C with a ramp rate of 30 °C/min (in N_2 atmosphere, ~10% RH), and 2D GIWAXS patterns were acquired during the heating cycle at every second at a fixed incident angle of 0.4°.

Materials Characterization

The UV-visible optical absorption spectra of perovskite thin films were acquired using a UV-visible spectrophotometer (Model Cary 60, Agilent, USA) with a scanning range of 300 nm to 800 nm and a scan rate of 1000 nm/min. Steady-state and time-resolved photoluminescence experiments were conducted with a Pharos ultrafast system and excitation wavelength of 640 nm. PL mapping was obtained with Olympus IX81 confocal microscope with 450 nm laser. The surface morphology of perovskite films was analyzed using SEM (Hitachi S4800) and contact-mode AFM (Bruker Dimension 3000) with a scan rate of 0.8 Hz to study the topological and surface roughness. The TEM images of exfoliated MoS_2 nanosheets were obtained using a JOEL 1400 TEM system, with acceleration voltage of 120 kV. XRD (Rigaku Ultima III) was used to collect crystallographic information. XPS measurements were carried out using a Physical Electronics Versa Probe II system with Al Kα X-ray source, 45° take-off angle, and low-energy electron and Ar+ surface charge compensation, under $5 \times 10^{-7} – 5 \times 10^{-8}$ Pa vacuum. XPS data analysis was done using Multipak, where the binding energy of the main C1s peak (284.8 eV) was used to correct the spectral shift caused by specimen charging. Raman measurement was acquired with Renishaw inVia Raman microscope and the data analysis was done with WIRE.

ToF-SIMS and TEM Characterization of FAPI PSCs

The distribution of added MoS_2 within the perovskite layer was examined by measuring the composition depth profile via ToF-SIMS (Physical Electronics, nanoTOF II). To clearly identify the top interface of the FAPI films, a thin layer of deuterated polystyrene (d-PS) was coated on top of the FAPI films. The depth profiles of positive ions (e.g., D^+, Pb+, Ti+, Mo+, etc.) were constructed by sputtering the samples using a 1 kV Ar gas gun (100 nA current, rastered over 1 mm × 1 mm area) and in sequence probing the composition of the exposed surface by using a 30 kV Bi^{3+} liquid metal ion beam and analyzing the generated secondary ions across a 100 μm × 100 μm area. Detailed atomic-scale structures of perovskite films were examined by scanning TEM (STEM FEI Talos and Hitachi HD2700C). Cross-sectional STEM samples were prepared via a standard lift-off technique using a focused ion beam (FIB, Helios G5 UX) system.

Supporting Information

The Supporting Information is available free of charge at https://pubs.acs.org/doi/ High-resolution XPS spectra of S 2P and Mo 3d; SEM image of MPA-MoS_2; photographs of MPA-MoS_2 dispersion; representative photovoltaic J-V characteristics with varying MPA-MoS_2 concentration and corresponding average photovoltaic parameters; statistics of photovoltaic parameters of FAPI PSCs with different MoS_2 additive conditions; representative forward-scan photovoltaic J-V characteristics with and without MPA-MoS_2 and corresponding EQE spectra; representative photovoltaic J-V curves of PSCs with MoS_2 and corresponding steady-state PCE and Jsc; top-view SEM images of FAPI films with different MoS_2 additive conditions and corresponding XRD spectra, associated crystallite sizes, and TRPL spectra and lifetimes; top-view AFM images of FAPI films with different MoS_2 additive conditions and corresponding optical absorption and PL spectra, and PL lifetime spatial mapping data; high-resolution XPS spectra of I 3d, N 1s, and C 1s spectra of FAPI with and without MPA-MoS_2; ex-situ GIWAXS data from a FAPI/MoS_2 sample with varying X-ray incident angles; HAADF cross-sectional STEM image and corresponding EDS elemental mapping data from FAPI/MPA-MoS_2 film; azimuthal GIWAXS intensity plots along the α(100) planes in FAPI with and without MoS_2; representative photovoltaic J-V curves (reverse scan) of the FAPI PSCs with MoS_2 additive conditions with PTAA as hole transport layer and corresponding average photovoltaic

parameters; temporal evolution of XRD spectra at 85 °C in Ar from FAPI with and without MPA-MoS_2; PCE evolution of non-encapsulated FAPI/MoS_2 PSCs under ambient, 85°C in Ar, and AM 1.5G light soaking in Ar.

Acknowledgement

This research was performed at the Materials Synthesis and Characterization, and Electron Microscopy Facilities of the Center for Functional Nanomaterials (CFN), and at the Complex Materials Scattering (CMS) beamline of National Synchrotron Light Source II (NSLS-II), which are U.S. Department of Energy Office of Science User Facilities, at Brookhaven National Laboratory under Contract No. DE-SC0012704. The research was also supported by the Office of Naval Research under Contract No. N000142012858. The authors acknowledge the use of the facilities at the Advanced Science Research Center (ASRC) at the City University of New York, and the Advanced Energy Research and Technology Center (AERTC) at Stony Brook University.

References

1. Shi, D.; Adinolfi, V.; Comin, R.; Yuan, M.; Alarousu, E.; Buin, A.; Chen, Y.; Hoogland, S.; Rothenberger, A.; Katsiev, K.; Losovyj, Y.; Zhang, X.; Dowben, P. A.; Mohammed, O. F.; Sargent, E. H.; Bakr, O. M., Low trap-state density and long carrier diffusion in organolead trihalide perovskite single crystals. *Science* **2015,** *347* (6221), 519-522.
2. Eperon, G. E.; Stranks, S. D.; Menelaou, C.; Johnston, M. B.; Herz, L. M.; Snaith, H. J., Formamidinium lead trihalide: a broadly tunable perovskite for efficient planar heterojunction solar cells. *Energy & Environmental Science* **2014,** *7* (3), 982-988.
3. Park, N.-G.; Zhu, K., Scalable fabrication and coating methods for perovskite solar cells and solar modules. *Nature Reviews Materials* **2020,** *5* (5), 333-350.
4. Jeon, N. J.; Noh, J. H.; Yang, W. S.; Kim, Y. C.; Ryu, S.; Seo, J.; Seok, S. I., Compositional engineering of perovskite materials for high-performance solar cells. *Nature* **2015,** *517* (7535), 476-480.
5. Kojima, A.; Teshima, K.; Shirai, Y.; Miyasaka, T., Organometal halide perovskites as visible-light sensitizers for photovoltaic cells. *J Am Chem Soc* **2009,** *131* (17), 6050-1.
6. Lu, H.; Liu, Y.; Ahlawat, P.; Mishra, A.; Tress, W. R.; Eickemeyer, F. T.; Yang, Y.; Fu, F.; Wang, Z.; Avalos, C. E.; Carlsen, B. I.; Agarwalla, A.; Zhang, X.; Li, X.; Zhan, Y.; Zakeeruddin, S. M.; Emsley, L.; Rothlisberger, U.; Zheng, L.; Hagfeldt, A.; Grätzel, M., Vapor-assisted deposition of highly efficient, stable black-phase FAPbI₃ perovskite solar cells. *Science* **2020,** *370* (6512), eabb8985.
7. Pellet, N.; Gao, P.; Gregori, G.; Yang, T.-Y.; Nazeeruddin, M. K.; Maier, J.; Grätzel, M., Mixed-Organic-Cation Perovskite Photovoltaics for Enhanced Solar-Light Harvesting. *Angewandte Chemie International Edition* **2014,** *53* (12), 3151-3157.

8. Chen, H.; Chen, Y.; Zhang, T.; Liu, X.; Wang, X.; Zhao, Y., Advances to High-Performance Black-Phase FAPbI3 Perovskite for Efficient and Stable Photovoltaics. *Small Structures* **2021,** *2* (5), 2000130.
9. Yao, D.; Zhang, C.; Pham, N. D.; Zhang, Y.; Tiong, V. T.; Du, A.; Shen, Q.; Wilson, G. J.; Wang, H., Hindered Formation of Photoinactive δ-FAPbI3 Phase and Hysteresis-Free Mixed-Cation Planar Heterojunction Perovskite Solar Cells with Enhanced Efficiency via Potassium Incorporation. *The Journal of Physical Chemistry Letters* **2018,** *9* (8), 2113-2120.
10. Han, Q.; Bae, S.-H.; Sun, P.; Hsieh, Y.-T.; Yang, Y.; Rim, Y. S.; Zhao, H.; Chen, Q.; Shi, W.; Li, G.; Yang, Y., Single Crystal Formamidinium Lead Iodide (FAPbI3): Insight into the Structural, Optical, and Electrical Properties. *Advanced Materials* **2016,** *28* (11), 2253-2258.
11. Li, G.; Zhang, T.; Xu, F.; Zhao, Y., A facile deposition of large grain and phase pure α-FAPbI3 for perovskite solar cells via a flash crystallization. *Materials Today Energy* **2017,** *5*, 293-298.
12. Ho, K.; Wei, M.; Sargent, E. H.; Walker, G. C., Grain Transformation and Degradation Mechanism of Formamidinium and Cesium Lead Iodide Perovskite under Humidity and Light. *ACS Energy Letters* **2021,** *6* (3), 934-940.
13. Yin, Y.; Zhou, Y.; Rafailovich, M. H.; Nam, C.-Y., Recent advances of two-dimensional material additives in hybrid perovskite solar cells. *Nanotechnology* **2023,** *34*, 172001.
14. Liu, Y.; Lee, S.; Yin, Y.; Li, M.; Cotlet, M.; Nam, C.-Y.; Lee, J.-K., Near-Band-Edge Enhancement in Perovskite Solar Cells via Tunable Surface Plasmons. *Advanced Optical Materials* **2022,** *10* (22), 2201116.
15. Zhou, Y.; Yin, Y.; Zuo, X.; Wang, L.; Li, T.-D.; Zhou, Y.; Padture, N. P.; Yang, Z.; Guo, Y.; Xue, Y.; Kisslinger, K.; Cotlet, M.; Nam, C.-Y.; Rafailovich, M. H., Enhancing Chemical Stability and Suppressing Ion Migration in CH3NH3PbI3 Perovskite Solar Cells via Direct Backbone Attachment of Polyesters on Grain Boundaries. *Chemistry of Materials* **2020,** *32* (12), 5104-5117.
16. Zhou, Y.; Tiwale, N.; Yin, Y.; Subramanian, A.; Rafailovich, M. H.; Nam, C.-Y., Effects of polymer grain boundary passivation on organic–inorganic hybrid perovskite field-effect transistors. *Applied Physics Letters* **2021,** *119* (18), 183303.
17. Zhou, Y.; Yin, Y.; Zuo, X.; Wang, L.; Li, T.-D.; Xue, Y.; Subramanian, A.; Fang, Y.; Guo, Y.; Yang, Z.; Cotlet, M.; Nam, C.-Y.; Rafailovich, M. H., Improving Thermal Stability of Perovskite Solar Cells by Suppressing Ion Migration Using Copolymer Grain Encapsulation. *Chemistry of Materials* **2021,** *33* (15), 6120-6135.
18. Salim, K. M. M.; Masi, S.; Gualdrón-Reyes, A. F.; Sánchez, R. S.; Barea, E. M.; Krecmarová, M.; Sánchez-Royo, J. F.; Mora-Seró, I., Boosting Long-Term Stability of Pure Formamidinium Perovskite Solar Cells by Ambient Air Additive Assisted Fabrication. *ACS Energy Letters* **2021,** *6* (10), 3511-3521.
19. Wang, Y.; Li, W.; Zhang, T.; Li, D.; Kan, M.; Wang, X.; Liu, X.; Wang, T.; Zhao, Y., Highly Efficient (110) Orientated FA-MA Mixed Cation Perovskite Solar Cells via Functionalized Carbon Nanotube and Methylammonium Chloride Additive. *Small Methods* **2020,** *4* (5), 1900511.
20. Yin, Z.; Li, H.; Li, H.; Jiang, L.; Shi, Y.; Sun, Y.; Lu, G.; Zhang, Q.; Chen, X.; Zhang, H., Single-Layer MoS2 Phototransistors. *ACS Nano* **2012,** *6* (1), 74-80.
21. Li, M.; Chen, J.-S.; Routh, P. K.; Zahl, P.; Nam, C.-Y.; Cotlet, M., Distinct Optoelectronic Signatures for Charge Transfer and Energy Transfer in Quantum Dot–MoS2 Hybrid Photodetectors Revealed by Photocurrent Imaging Microscopy. *Advanced Functional Materials* **2018,** *28* (29), 1707558.
22. Withers, F.; Del Pozo-Zamudio, O.; Mishchenko, A.; Rooney, A. P.; Gholinia, A.; Watanabe, K.; Taniguchi, T.; Haigh, S. J.; Geim, A. K.; Tartakovskii, A. I.; Novoselov, K. S., Light-emitting diodes by band-structure engineering in van der Waals heterostructures. *Nature Materials* **2015,** *14* (3), 301-306.
23. Chou, S. S.; De, M.; Kim, J.; Byun, S.; Dykstra, C.; Yu, J.; Huang, J.; Dravid, V. P., Ligand Conjugation of Chemically Exfoliated MoS2. *Journal of the American Chemical Society* **2013,** *135* (12), 4584-4587.

24. Backes, C.; Berner, N. C.; Chen, X.; Lafargue, P.; LaPlace, P.; Freeley, M.; Duesberg, G. S.; Coleman, J. N.; McDonald, A. R., Functionalization of Liquid-Exfoliated Two-Dimensional 2H-MoS2. *Angewandte Chemie International Edition* **2015,** *54* (9), 2638-2642.
25. Reinhart, C. C.; Johansson, E., Colloidally Prepared 3-Mercaptopropionic Acid Capped Lead Sulfide Quantum Dots. *Chemistry of Materials* **2015,** *27* (21), 7313-7320.
26. Tsai, D.-H.; DelRio, F. W.; MacCuspie, R. I.; Cho, T. J.; Zachariah, M. R.; Hackley, V. A., Competitive Adsorption of Thiolated Polyethylene Glycol and Mercaptopropionic Acid on Gold Nanoparticles Measured by Physical Characterization Methods. *Langmuir* **2010,** *26* (12), 10325-10333.
27. Kakavelakis, G.; Paradisanos, I.; Paci, B.; Generosi, A.; Papachatzakis, M.; Maksudov, T.; Najafi, L.; Del Rio Castillo, A. E.; Kioseoglou, G.; Stratakis, E.; Bonaccorso, F.; Kymakis, E., Extending the Continuous Operating Lifetime of Perovskite Solar Cells with a Molybdenum Disulfide Hole Extraction Interlayer. *Advanced Energy Materials* **2018,** *8* (12), 1702287.
28. Divigalpitiya, W. M. R.; Frindt, R. F.; Morrison, S. R., Inclusion Systems of Organic Molecules in Restacked Single-Layer Molybdenum Disulfide. *Science* **1989,** *246* (4928), 369-371.
29. Ali, S. R.; De, M., Thiolated Ligand-Functionalized MoS2 Nanosheets for Peroxidase-like Activities. *ACS Applied Nano Materials* **2021,** *4* (11), 12682-12689.
30. Mai, H. D.; Jeong, S.; Bae, G.-N.; Tran, N. M.; Youn, J.-S.; Park, C.-M.; Jeon, K.-J., Pd Sulfidation-Induced 1T-Phase Tuning in Monolayer MoS2 for Hydrogen Evolution Reaction. *Advanced Energy Materials* **2023,** *13* (23), 2300183.
31. Coleman, J. N.; Lotya, M.; O'Neill, A.; Bergin, S. D.; King, P. J.; Khan, U.; Young, K.; Gaucher, A.; De, S.; Smith, R. J.; Shvets, I. V.; Arora, S. K.; Stanton, G.; Kim, H.-Y.; Lee, K.; Kim, G. T.; Duesberg, G. S.; Hallam, T.; Boland, J. J.; Wang, J. J.; Donegan, J. F.; Grunlan, J. C.; Moriarty, G.; Shmeliov, A.; Nicholls, R. J.; Perkins, J. M.; Grieveson, E. M.; Theuwissen, K.; McComb, D. W.; Nellist, P. D.; Nicolosi, V., Two-Dimensional Nanosheets Produced by Liquid Exfoliation of Layered Materials. *Science* **2011,** *331* (6017), 568-571.
32. Glowienka, D.; Galagan, Y., Light Intensity Analysis of Photovoltaic Parameters for Perovskite Solar Cells. *Advanced Materials* **2022,** *34* (2), 2105920.
33. You, P.; Tang, G.; Cao, J.; Shen, D.; Ng, T.-W.; Hawash, Z.; Wang, N.; Liu, C.-K.; Lu, W.; Tai, Q.; Qi, Y.; Lee, C.-S.; Yan, F., 2D materials for conducting holes from grain boundaries in perovskite solar cells. *Light: Science & Applications* **2021,** *10* (1), 68.
34. Liu, Z.; Liu, K.; Zhang, F.; Jain, S. M.; He, T.; Jiang, Y.; Liu, P.; Yang, J.; Liu, H.; Yuan, M., CH3NH3PbI3:MoS2 heterostructure for stable and efficient inverted perovskite solar cell. *Solar Energy* **2020,** *195*, 436-445.
35. Xie, F.; Chen, C.-C.; Wu, Y.; Li, X.; Cai, M.; Liu, X.; Yang, X.; Han, L., Vertical recrystallization for highly efficient and stable formamidinium-based inverted-structure perovskite solar cells. *Energy & Environmental Science* **2017,** *10* (9), 1942-1949.
36. Zhang, F.; Shi, W.; Luo, J.; Pellet, N.; Yi, C.; Li, X.; Zhao, X.; Dennis, T. J. S.; Li, X.; Wang, S.; Xiao, Y.; Zakeeruddin, S. M.; Bi, D.; Grätzel, M., Isomer-Pure Bis-PCBM-Assisted Crystal Engineering of Perovskite Solar Cells Showing Excellent Efficiency and Stability. *Advanced Materials* **2017,** *29* (17), 1606806.
37. Zhang, G.; Bui, V.; Yin, Y.; Tsai, E. H. R.; Nam, C.-Y.; Lin, H., Carbon Capture Membranes Based on Amorphous Polyether Nanofilms Enabled by Thickness Confinement and Interfacial Engineering. *ACS Applied Materials & Interfaces* **2023,** *15* (29), 35543-35551.
38. Park, B.-w.; Kwon, H. W.; Lee, Y.; Lee, D. Y.; Kim, M. G.; Kim, G.; Kim, K.-j.; Kim, Y. K.; Im, J.; Shin, T. J.; Seok, S. I., Stabilization of formamidinium lead triiodide α-phase with isopropylammonium chloride for perovskite solar cells. *Nature Energy* **2021,** *6* (4), 419-428.

39. Kim, S.; Lee, Y. J.; Park, J. D.; Kang, G.; Park, M., Selective Passivation of Grain Boundaries via Incorporation of a Fluidic Small Molecule in Perovskite Solar Absorbers. *ACS Applied Energy Materials* **2021,** *4* (9), 10059-10068.
40. Deng, Y.-H., Common Phase and Structure Misidentifications in High-Resolution TEM Characterization of Perovskite Materials. *Condensed Matter* **2021,** *6* (1), 1.
41. Gao, D.; Si, M.; Li, J.; Zhang, J.; Zhang, Z.; Yang, Z.; Xue, D., Ferromagnetism in freestanding MoS2 nanosheets. *Nanoscale Research Letters* **2013,** *8* (1), 129.
42. Yin, Y.; Zhou, Y.; Fu, S.; Zuo, X.; Lin, Y.-C.; Wang, L.; Xue, Y.; Zhang, Y.; Tsai, E. H. R.; Hwang, S.; Kissenger, K.; Li, M.; Cotlet, M.; Li, T.-D.; Yager, K. G.; Nam, C.-Y.; Rafailovich, M. H., Enhancing Crystallization in Hybrid Perovskite Solar Cells Using Thermally Conductive 2D Boron Nitride Nanosheet Additive. *Small* **2023,** *19* (15), 2207092.
43. Masi, S.; Gualdrón-Reyes, A. F.; Mora-Seró, I., Stabilization of Black Perovskite Phase in FAPbI3 and CsPbI3. *ACS Energy Letters* **2020,** *5* (6), 1974-1985.
44. Kim, M.; Kim, G.-H.; Lee, T. K.; Choi, I. W.; Choi, H. W.; Jo, Y.; Yoon, Y. J.; Kim, J. W.; Lee, J.; Huh, D.; Lee, H.; Kwak, S. K.; Kim, J. Y.; Kim, D. S., Methylammonium Chloride Induces Intermediate Phase Stabilization for Efficient Perovskite Solar Cells. *Joule* **2019,** *3* (9), 2179-2192.
45. Chen, T.; Foley, B. J.; Park, C.; Brown, C. M.; Harriger, L. W.; Lee, J.; Ruff, J.; Yoon, M.; Choi, J. J.; Lee, S.-H., Entropy-driven structural transition and kinetic trapping in formamidinium lead iodide perovskite. *Science Advances* **2016,** *2* (10), e1601650.
46. Tang, G.; You, P.; Tai, Q.; Yang, A.; Cao, J.; Zheng, F.; Zhou, Z.; Zhao, J.; Chan, P. K. L.; Yan, F., Solution-Phase Epitaxial Growth of Perovskite Films on 2D Material Flakes for High-Performance Solar Cells. *Advanced Materials* **2019,** *31* (24), 1807689.
47. Cao, J.; Tang, G.; You, P.; Wang, T.; Zheng, F.; Zhao, J.; Yan, F., Enhanced Performance of Planar Perovskite Solar Cells Induced by Van Der Waals Epitaxial Growth of Mixed Perovskite Films on WS2 Flakes. *Advanced Functional Materials* **2020,** *30* (38), 2002358.
48. Zheng, D.; Raffin, F.; Volovitch, P.; Pauporté, T., Control of perovskite film crystallization and growth direction to target homogeneous monolithic structures. *Nature Communications* **2022,** *13* (1), 6655.
49. Yang, Z.; Guo, Y.; Li, H.; Zhou, Y.; Zuo, X.; Yu, Y.; Pan, C.; Strzalka, J.; Nam, C.-Y.; Rafailovich, M. H., Roles of Interfacial Tension in Regulating Internal Organization of Low Bandgap Polymer Bulk Heterojunction Solar Cells by Polymer Additives. *Advanced Materials Interfaces* **2018,** *5* (15), 1800435.

ToC graphic